CrossMark
click for updates

1D/2D CeO₂/ZnIn₂S₄ Z-scheme heterojunction photocatalysts for efficient H₂ evolution under visible light

Renqian Jiang[1,2], Liang Mao[1,2], Yulong Zhao[1,2], Junying Zhang[3], Eugene B. Chubenko[4], Vitaly Bondarenko[4], Yanwei Sui[1,2], Xiuquan Gu[1,2*] and Xiaoyan Cai[1,2*]

ABSTRACT The development of a high-efficiency photocatalyst having favorable charge transfer has become an important scientific approach for solar-to-fuel conversion. In this study, the one-dimensional (1D)/2D CeO₂/ZnIn₂S₄ (ZIS) photocatalyst having a Z-scheme heterojunction has been successfully fabricated using the *in situ* growth of ZIS nanosheets on the CeO₂ nanorod surfaces. The optimal H₂ production rate of 3.29 mmol g⁻¹ h⁻¹ was achieved with the 15% CeO₂/ZIS sample under visible light without any cocatalyst; furthermore, this value was 2.7 and 92.6 times higher than those of pristine ZIS and CeO₂, respectively. The remarkable photocatalytic activity can be attributed to the efficient separation of photogenerated carriers as well as the formation of the Z-scheme heterojunction, which maintained the strong reduction of electrons in ZIS for H₂ production. The presence of an internal electric field between CeO₂ and ZIS has been demonstrated by both density functional theory calculations and Kelvin probe force microscopy. The Z-scheme transfer of photogenerated carriers in the CeO₂/ZIS heterojunction has been confirmed by electron paramagnetic resonance spectroscopy and *in situ* irradiated X-ray photoelectron spectroscopy. This study presents certain insights into the development of efficient Z-scheme photocatalysts for H₂ evolution from solar water splitting.

Keywords: photocatalyst, ZnIn₂S₄, Z-scheme, hydrogen evolution, solar fuel

INTRODUCTION

With the increase in energy demand, researchers around the world are eager to identify new ways to access renewable energy [1–3]. Because of its unlimited resource potential, hydrogen generation by solar water splitting is considered an efficient approach for overcoming the energy crisis and environmental pollution of the past few decades [4–6]. Since first discovered by Fujishima and Honda [7] in 1972, H₂ production from water splitting using particulate semiconductor photocatalysts has attracted considerable attention because it is eco-friendly and inexpensive [8–10].

Among emerging photocatalysts, hexagonal-phased ZnIn₂S₄ (ZIS), as an important n-type semiconductor with an appropriate bandgap (~2.4 eV), has attracted considerable attention [11,12]. The unique two-dimensional (2D) layered structure, excellent photocatalytic stability [13], and nontoxicity [14] of ZIS make it an ideal candidate for the photocatalytic H₂ evolution reaction (HER) [15]. However, the HER efficiency of ZIS remains unsatisfactory primarily because of the high recombination rate of photogenerated carriers [16]. To date, many strategies have been employed to enhance the HER performance of ZIS, including elemental modification [17,18], the use of cocatalysts [19], and heterojunction manipulation [20,21].

Two primary types of heterojunctions that increase the photocatalytic activity of ZIS, namely, Type II and Z-scheme heterojunctions, are extensively acknowledged [22–24]. The Z-scheme heterojunction offers the advantages of overall water splitting or H₂ evolution with hole scavenger in water under visible light irradiation because the high redox capabilities of two semiconductor components are preserved, and efficient spatial separation of photoinduced carriers is achieved [25–27]. Typically, the modern Z-scheme system is composed of an oxidizing photocatalyst (OP) with a low valence band (VB) position and a reducing photocatalyst (RP) with a high conduction band (CB) position. When they remain in contact, electrons in RP will transfer to OP across their interfaces, resulting in the formation of an internal electric field from RP to OP. Under the internal electric field, the "useless" electrons in the CB of OP and the "useless" holes in the VB of RP are recombined, whereas the holes in the VB of OP and the electrons in the CB of RP are retained, leading to the efficient separation of photogenerated electrons and holes in space [28]. Luo *et al.* [29] reported the fabrication of a flexible ultrathin WO₃₋ₓ/ZIS Z-scheme heterojunction photocatalyst using the mild oil bath method, leading to a 3.23-times increase in the photocatalytic H₂ production rate. They confirmed the Z-scheme carrier transfer *via* theoretical calculations and experimental evidence. For ZIS, a suitable analog for realizing Z-scheme transfer that can achieve effective separation of photogenerated carriers with no loss in the H₂ evolution rate needs to be identified [30]. According to previous studies, the CB and VB

1 School of Materials Science and Physics, China University of Mining and Technology, Xuzhou 221116, China
2 Jiangsu Province Engineering Laboratory of High Efficient Energy Storage Technology and Equipment, Xuzhou 221116, China
3 School of Physics, Beihang University, Beijing 100191, China
4 Micro- and Nanoelectronics Department, Belarusian State University of Informatics and Radioelectronics, Minsk 220013, Belarus
* Corresponding authors (emails: xqgu@cumt.edu.cn (Gu X); xycai@cumt.edu.cn (Cai X))

potentials of ZIS and CeO₂ are approximately −0.73 and 1.67 eV and approximately −0.44 and 2.56 eV, respectively [31,32]. A Z-scheme heterojunction can be generated between them, resulting in highly efficient charge separation. Moreover, with its strong electronic interaction, CeO₂ is often selected to be an important component for HER catalyst fabrication [33]. Therefore, its unique physical/chemical properties and suitable bandgap make it a promising photocatalyst that can be combined with ZIS to achieve enhanced HER activity [34,35].

In this study, a CeO₂/ZIS core-shell heterostructure was developed by *in situ* growth of ultrathin ZIS nanosheets (NSs) on the CeO₂ nanorod (NR) surface. The CeO₂/ZIS Z-scheme heterojunction was investigated by a comprehensive analysis based on both experimental evidence and theoretical calculations. In particular, certain *in situ* characterizations (such as Kelvin probe force microscopy (KPFM) and *in situ* irradiated X-ray photoelectron spectroscopy (XPS)) were used to reveal the charge transfer in the CeO₂/ZIS heterojunction as per the Z-scheme, which ensured the simultaneous enhancement of visible light absorption, charge separation, and redox capability. Consequently, the CeO₂/ZIS photocatalyst exhibits a higher photocatalytic H₂ performance compared with single ZIS or CeO₂ under visible light irradiation. Our study will provide a new reference for designing and developing high-efficiency photocatalysts for H₂ evolution.

EXPERIMENTAL

Chemicals

Zinc chloride (ZnCl₂, AR), indium(III) chloride (InCl₃, 98%), NaOH, and thioacetamide (CH₃CSNH₂, TAA, AR) were obtained from Rhawn Chemical Reagent Co., Ltd. Cerium(III) chloride heptahydrate (CeCl₃·7H₂O, AR) was purchased from Shanghai Xianding Biotechnology Co., Ltd. All reagents were then used without additional purification.

Synthesis of CeO₂ NRs

For a typical experiment, 0.5 g of CeCl₃·7H₂O and 40 mL of 10 mol L⁻¹ NaOH solution were placed in a 100-mL Teflon-lined autoclave and vigorously stirred. Then, the autoclave was sealed and maintained at 130°C for 15 h. When the reaction system was cooled to room temperature (RT), the precipitate was washed with deionized (DI) water and dried in a vacuum at 50°C. Subsequently, the as-prepared Ce(OH)₃ powders were dispersed in DI water, mixed with 15% H₂O₂, and stirred for 2 h. Finally, the CeO₂ NRs were collected by centrifugation, washed thoroughly with DI water, and dried at 50°C for further use.

Synthesis of CeO₂/ZIS composites

CeO₂/ZIS composites were prepared using an oil bath method. Typically, the obtained CeO₂ NRs (with CeO₂/ZIS weight ratios of 10/90, 15/85, and 20/80) were dispersed in 30 mL of H₂O (pH 2.5) and stirred for 20 min. Subsequently, 0.0816 g ZnCl₂, 0.1326 g InCl₃, and 0.09 g TAA were added to the aforementioned mixture and continuously stirred for 20 min to obtain a uniform suspension. Then, the mixture was heated at 80°C for 2 h using an oil bath. After cooling to RT, the obtained solid products were washed several times with ethanol and dried at 50°C for 1 h. The as-synthesized CeO₂/ZIS composites with 10, 15, and 20 wt% CeO₂ loadings were labeled as 10% CeO₂/ZIS, 15% CeO₂/ZIS, and 20% CeO₂/ZIS, respectively. For compar-

ison, pure ZIS was prepared using the same route without the addition of CeO₂ NRs.

Material characterization

The crystalline phases of samples were characterized using X-ray diffraction (XRD; Bruker D8 Advance) with Cu Kα radiation (λ = 1.54056 Å). The sample morphologies were characterized using a field-emission scanning electron microscope (SEM; Hitachi New Generation SU8220) with an accelerating voltage of 5.0 kV and a transmission electron microscope (TEM; Tecnai G2 F20) with an accelerating voltage of 300 kV. XPS (Thermo Fisher Scientific) with the monochromatic Al Kα radiation (200 W) was used to determine the surface chemical valence states of the prepared photocatalysts. The *in situ* XPS experiments were performed under simultaneous 450-nm light-emitting diode (LED) irradiation. The light diffusion absorption properties of samples were investigated using the Cary 300 ultraviolet-visible (UV-vis) diffuse reflectance spectrophotometer (DRS) using BaSO₄ as the reference background. The steady-state photoluminescence (PL) and time-resolved PL (TRPL) were obtained by the fluorescence spectrometer (Edinburgh FS5) equipped with a Xe lamp. The average TRPL lifetime (Ave. τ) was calculated using the following formula:

$$\tau = \left(A_1 \tau_1^2 + A_2 \tau_2^2 \right) / \left(A_1 \tau_1 + A_2 \tau_2 \right). \tag{1}$$

where τ_i and A_i are the lifetime and associated amplitude of the exponential decay fit, respectively. The electron paramagnetic resonance (EPR) spectra were obtained using an EPR spectrometer (A300, Bruker, UK) with a modulation amplitude of 1 G and microwave power of 3.99 mW. Atomic force microscopy (AFM) and KPFM (Bruker Nano Inc.) were used to characterize the surface morphology and potential of samples, respectively.

Photocatalytic measurements for H₂ evolution

The photocatalytic HER performance of CeO₂/ZIS hybrid photocatalysts was evaluated using a 300-W Xe lamp (λ > 420 nm) as the visible light irradiation source. The powder samples (10 mg) were mixed with 3 mL methanol (a hole sacrificial agent) and 12 mL DI water and stirred for 30 min to ensure homogeneity. Before irradiation, the reaction system was evacuated for ~30 min to remove air. During irradiation, the dispersion was maintained at ~25°C with a flow of cooling water. Every 30 min, 500 μL of photoreacted gas was extracted and injected into a gas chromatograph (Shimadzu GC-2030) equipped with a thermal conductivity detector to measure the amount of generated H₂. The apparent quantum efficiency (AQE) of the sample was then estimated using Equation (2):

$$\text{AQE} = \frac{2 \times \text{number of evolved hydrogen molecules}}{\text{number of incident photons}}$$
$$\times 100\%. \tag{2}$$

Photocatalytic degradation measurements

A 300-W Xe lamp (λ > 420 nm) was used as the visible light irradiation source. The photocatalyst (10 mg) was then added to the 10 mg L⁻¹ methylene blue (MB) solution (50 mL) and stirred for 30 min in the dark to form an adsorption-desorption equilibrium suspension. During the test, 3 mL of the MB solution was centrifuged every 30 min to collect the supernatant for UV-vis absorbance measurements. The change in the MB concentration during the photodegradation process can be eval-

uated by monitoring absorbance at 664 nm.

Photoelectrochemical measurements
In this work, the photocatalyst suspension (i.e., 10 mg sample mixed with 10 μL of H$_2$O, 10 μL of ethanol, and 5 μL of the 5% Nafion solution) was deposited on the 2 cm × 1 cm fluorine-doped tin oxide (FTO) glass electrode as the working electrode (the coated area is 1 cm^2). A Pt foil was employed as the counter electrode, and a saturated calomel electrode was used as the reference electrode. A 500-W Xe lamp was utilized as the irradiation source in the photoelectrocatalysis (PEC) measurements. The PEC properties (including the photocurrent *vs.* time (*I-t*)), Mott-Schottky (M-S) plots, and electrochemical impedance spectroscopy (EIS) data were recorded using the CHI-660E electrochemical workstation (ChenHua Instrument Co. Ltd.) with a conventional three-electrode system and 0.5 mol L^{-1} Na$_2$SO$_4$ aqueous electrolyte.

Computational details
All material simulations were conducted in the CASTEP mode of Materials Studio as per the density functional theory (DFT).

The interaction between valence electrons and the ionic core was described using the ultrasoft pseudopotential. The exchange-correlation functional in the Perdew-Burke-Ernzerhof form was used for the generalized gradient approximation. The geometry optimization and electrostatic potential calculations were then completed using the cutoff energy of 320 eV and Monkhorst-Pack grids of 6 × 4 × 1 for the CeO$_2$ crystal and 3 × 3 × 1 for the ZIS. The convergence thresholds for geometry optimization were set as 5.0 × 10^{-6} eV atom^{-1} for energy, 0.01 eV Å^{-1} for maximum force, and 0.02 GPa for maximum stress.

RESULTS AND DISCUSSION

XRD and TEM analyses
The crystal structures of the prepared samples were investigated using XRD, as shown in Fig. S1 and Fig. 1a. Ce(OH)$_3$ NRs were synthesized as per the reported method (Scheme 1) [36]. Fig. S1a shows that the majority of the characteristic diffraction peaks of Ce(OH)$_3$ are consistent with those of the well-crystallized hexagonal Ce(OH)$_3$ (JCPDS No. 74-0665) [36], whereas the peaks at 2θ = 33.08° are attributed to the (200) crystallographic planes of
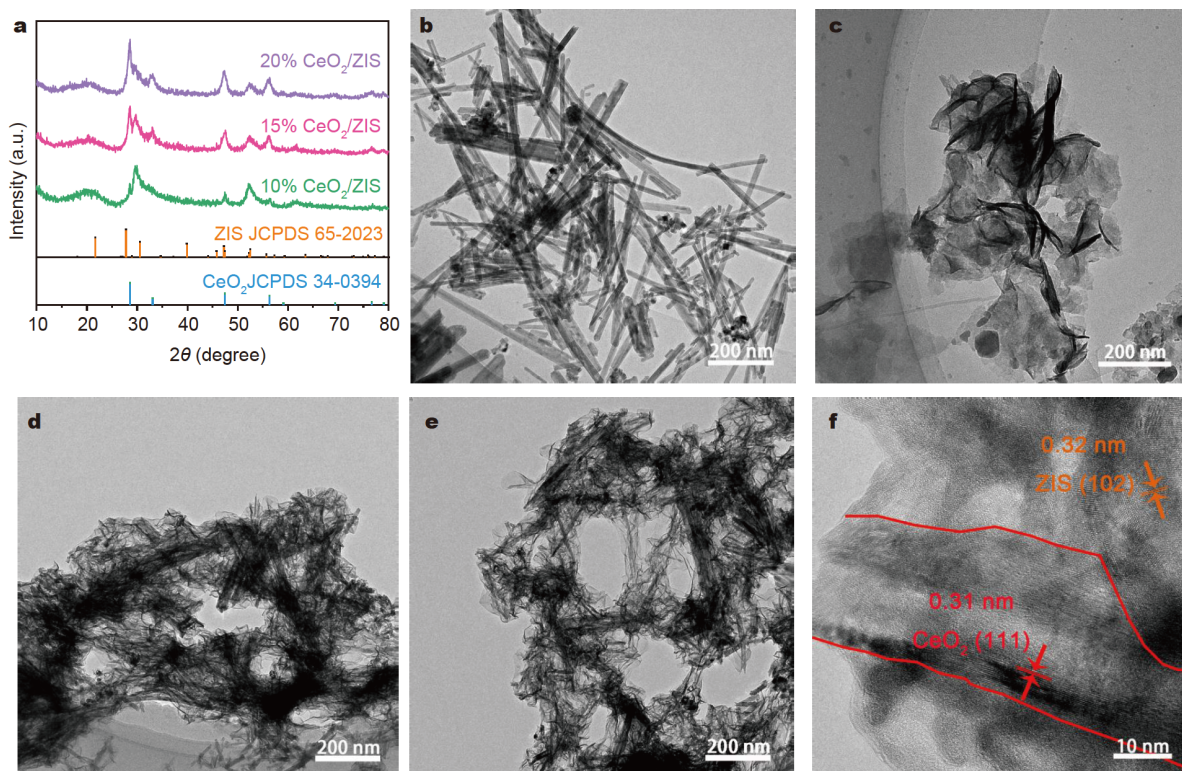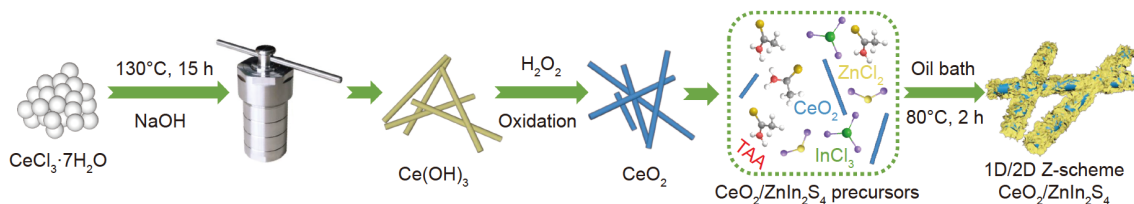

Figure 1 (a) XRD patterns of CeO$_2$/ZIS samples with various compositions. TEM images of (b) pure CeO$_2$ NRs, (c) pure ZIS NSs, and (d, e) CeO$_2$/ZIS hybrids. (f) HRTEM images of CeO$_2$/ZIS hybrids.

Scheme 1 Schematic of the synthesis process of the CeO$_2$/ZIS heterojunction.

CeO_2 [37]. $Ce(OH)_3$ is partially oxidized in air. After H_2O_2 oxidation treatment, $Ce(OH)_3$ can be completely converted into CeO_2 with the peaks at $2\theta = 28.55°$, $33.08°$, $47.48°$, $56.33°$, and $59.09°$, corresponding to the (111), (200), (220), (311), and (222) faces of cubic CeO_2 (JCPDS No. 34-0394) [38]. For pure ZIS (Fig. S1b), all of the diffraction peaks can be attributed to the hexagonal-phased ZIS (JCPDS No. 65-2023) [39]. Furthermore, the XRD patterns of CeO_2/ZIS composites (Fig. 1a) are similar to those of pure ZIS, except for two peaks of CeO_2 at 28.55° and 59.09° because of the low content of CeO_2. Note that the intensity of the two peaks of the CeO_2/ZIS samples could be strengthened with the increase of the CeO_2 content. Then, the morphology of samples was examined by SEM, TEM, and high-resolution TEM (HRTEM). As shown in Fig. S2a, b, both $Ce(OH)_3$ and CeO_2 samples exhibit rod-like structures with diameters of 10–20 nm and lengths of tens to hundreds of nanometers. As shown in Fig. S2c, f, the ZIS NSs are crystallized in ultrathin NSs, whereas the morphology of the CeO_2/ZIS samples seems to be the same as that of pure ZIS, which can be attributed to the low amount of CeO_2. All elements, including Zn, In, S, Ce, and O, are uniformly distributed throughout the particle (Fig. S3). The NR structure of CeO_2 and the NS structure of ZIS are detected as shown in Fig. 1b, c, respectively, which agrees with the SEM observations. As shown in Fig. 1d, e, the hierarchical structure of CeO_2/ZIS can be clearly observed in the TEM image, indicating intimate contact between CeO_2 and ZIS. Fig. 1f shows two sets of lattices with spaces of 0.31 and 0.32 nm, which can be attributed to the (111) plane of CeO_2 and the (102) plane of ZIS, respectively [40]. Moreover, the rod-like CeO_2 is decorated with ultrathin ZIS NSs, indicating close contact between ZIS and CeO_2.

Band structure

The optical absorption properties were examined using UV-vis DRS. As shown in Fig. 2a, pristine ZIS has an absorption edge at ~510 nm, whereas CeO_2 has an absorption edge at ~484 nm, which is consistent with previous studies. The absorption edge of CeO_2/ZIS is practically unchanged compared with that of ZIS, probably because the optical absorption of ZIS is dominant in the hierarchically structured composite. Note that the absorption of the hybrid sample in the UV region is weaker than that of CeO_2 and ZIS, which can be attributed to measurement/instrument error. Fig. S4 shows the band structure of ZIS and CeO_2. ZIS is a direct bandgap semiconductor, whereas CeO_2 is an indirect bandgap semiconductor. The plot of $(\alpha h\nu)^2$ vs. photon energy ($h\nu$) was used to determine the bandgap energy (E_g) of the samples. As shown in Fig. 2b, c, the bandgap values of ZIS and CeO_2 are 2.45 and 2.67 eV, respectively. Moreover, Fig. 2d shows that both ZIS and CeO_2 are n-type semiconductors with positive slopes; thus, their flat-band potentials (V_{fb}) are nearly identical to the Fermi level (E_f) [41,42]. The derived V_{fb} of ZIS and CeO_2 is calculated to be approximately −0.71 and −0.18 V vs. the reversible hydrogen electrode (RHE), respectively. The VB potential (E_{VB}) and E_f of ZIS, CeO_2, and CeO_2/ZIS can be confirmed by ultraviolet photoelectron spectroscopy (UPS), as shown in Fig. 2e–g, respectively. E_f of ZIS and CeO_2 is estimated to be −0.73 and −0.19 eV vs. RHE, which is consistent with the M-S test results. E_f of CeO_2/ZIS (−0.41 eV vs. RHE) is located between ZIS and CeO_2, revealing Fermi level equilibration after their combination. The chemical potential (=Fermi level) within the N–N junction is balanced to be equal to the charge transfer of the constituents; therefore, the overall apparent E_g will be smaller than that of the individual apparent E_g. In this study, the individual apparent E_g reveals a largely Z-scheme heterojunction. Then, the E_{VB} values of ZIS and CeO_2 are calculated to be 1.56 and 2.08 eV vs. RHE, respectively. By combining the bandgap values with their VB positions, we can deduce that the conductive band potentials (E_{CB}) of ZIS and CeO_2 are approximately −0.89 and −0.59 eV vs. RHE, respectively. Based on the aforementioned results, the band structures of ZIS and CeO_2 can be determined (Fig. 2h).

Photocatalytic performance

Fig. 3a, b show the photocatalytic HER performances of pure CeO_2, ZIS, and CeO_2/ZIS heterojunctions with different ratios of methanol under visible light ($\lambda > 400$ nm) irradiation. Note that pure CeO_2 exhibits poor photocatalytic performance for H_2 production because of its low E_{CB}. ZIS shows a weak photo-
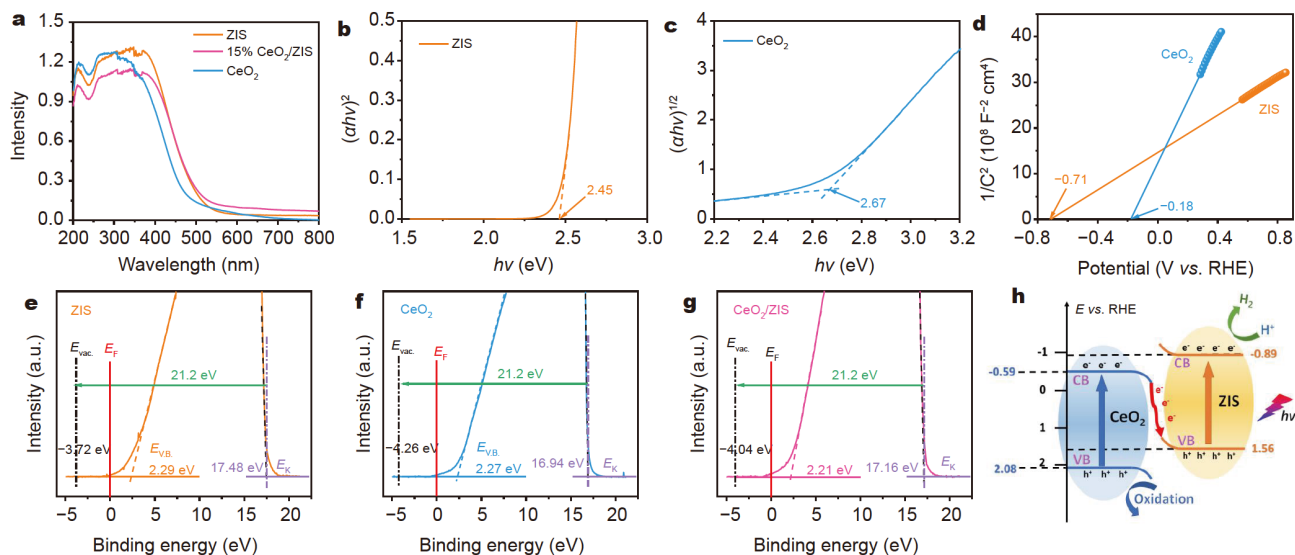

Figure 2 (a) UV-vis spectra and Tauc plots of $(\alpha h\nu)^2$ vs. photon energy ($h\nu$) for determining the bandgaps of (b) ZIS and (c) CeO_2. (d) M-S plots of ZIS and CeO_2. UPS spectra of (e) ZIS, (f) CeO_2, and (g) CeO_2/ZIS. (h) Band structures of the pure ZIS and CeO_2 samples.
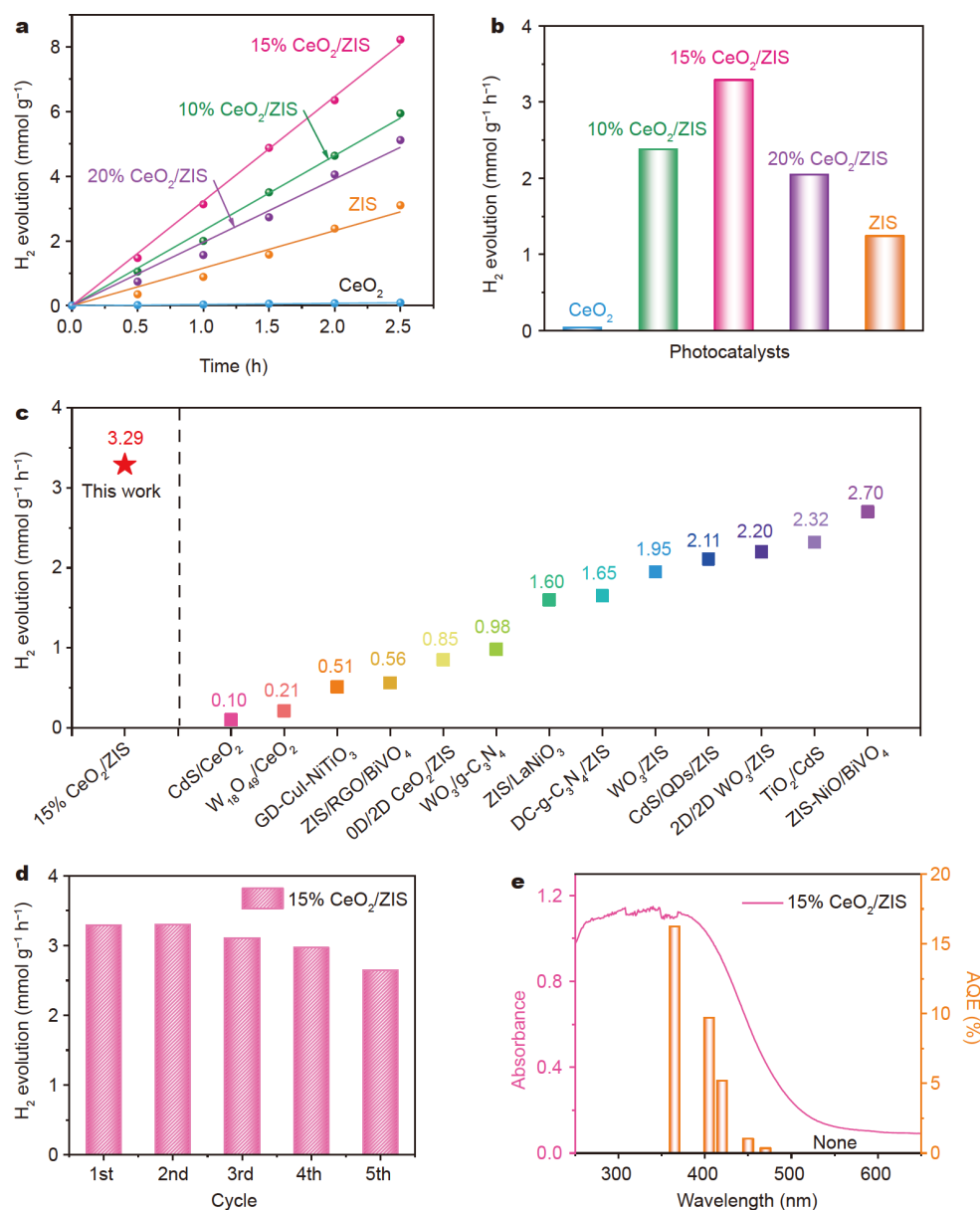
Figure 3 (a) Time course for H_2 evolution and (b) apparent photocatalytic H_2 evolution rates of CeO_2, ZIS, and CeO_2/ZIS under visible light. (c) Comparison of the reported H_2 evolution rates of Z-scheme or S-scheme photocatalysts with this work. (d) Cycle stability test of H_2 evolution. (e) UV-vis absorption spectrum and AQE of 15% CeO_2/ZIS.

catalytic activity with the H_2 evolution rate of 1.24 mmol g^{-1} h^{-1}, which can be attributed to the high recombination of photo-generated charges. As expected, the capability to produce H_2 remarkably increases when CeO_2 is combined with ZIS. The 15% CeO_2/ZIS exhibits the highest HER value of 3.29 mmol g^{-1} h^{-1}, which is ~2.7 and 92.6 times higher than those of pristine ZIS and CeO_2, respectively. The HER rate decreases when the CeO_2 content in the hybrid is increased to 20 wt%, which can be attributed to the inevitable recombination of photogenerated electrons and holes in the superfluous ZIS clusters before the redox reaction. Moreover, the optimal HER performance in the present work is superior to those in previous reports on Z-scheme photocatalysts (Fig. 3c and Table S1). As shown in Fig. 3d, the photostability of the 15% CeO_2/ZIS catalyst was evaluated under visible light irradiation for 12.5 h. After five cycles, the photocatalytic HER value of the 15% CeO_2/ZIS

sample can retain 2.65 mmol g^{-1} h^{-1}, indicating the good stability of the as-prepared Z-scheme photocatalyst. For the recycled 15% CeO_2/ZIS sample, no obvious changes in either morphology or crystal structure are observed even after 12.5 h of photocatalytic test (Figs S5 and S6). Fig. 3e shows the AQE values of the 15% CeO_2/ZIS sample at different wavelengths of incident light. The AQE plot of CeO_2/ZIS is consistent with the UV-vis absorption spectra, with the AQE values of 16.23% achieved at 365 nm and 9.70% achieved at 405 nm.

PL spectra and PEC performance
The charge carrier dynamics of the samples were investigated using PL and TRPL (Fig. 4a, b). The 15% CeO_2/ZIS sample shows a remarkable fluorescence quenching compared with the CeO_2 and ZIS samples, indicating a highly efficient charge separation (Fig. 4a). The TRPL spectra (Fig. 4b) show that 15%
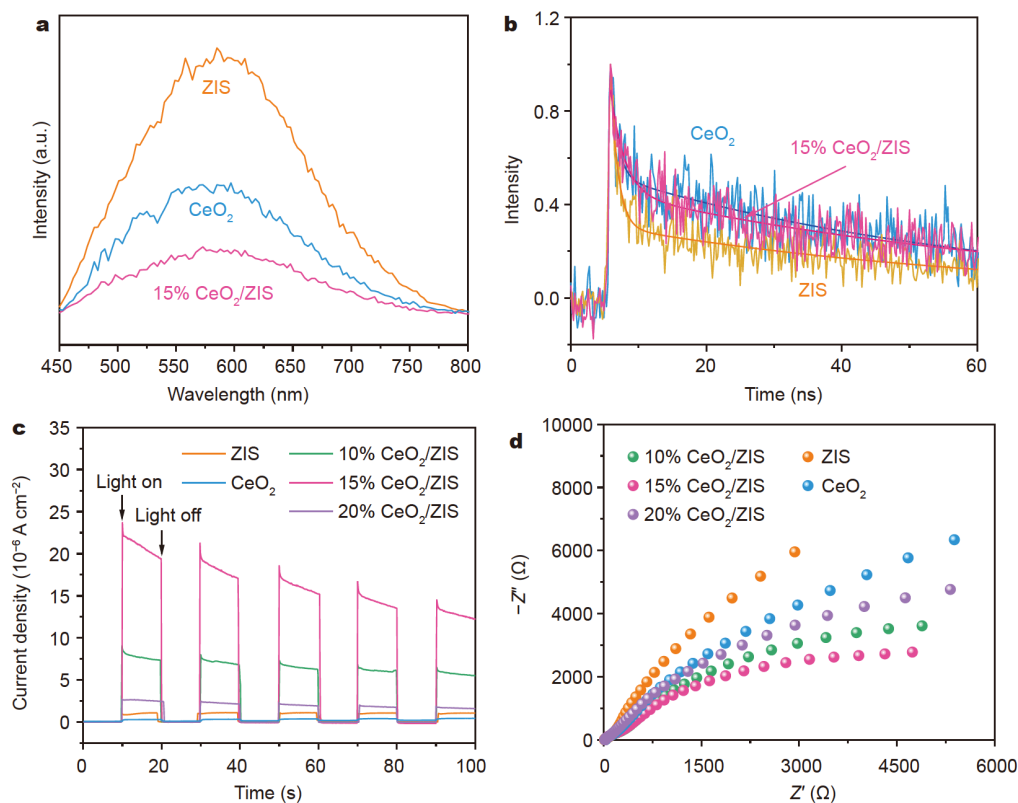
Figure 4 (a) Steady-state PL spectra, (b) time-resolved transient PL spectra, (c) *I-t* plots, and (d) EIS plots of CeO_2, ZIS, and 15% CeO_2/ZIS.

CeO_2/ZIS exhibits a longer average lifetime (i.e., 74.32 ns) than ZIS (67.17 ns) and CeO_2 (56.25 ns; Table S2), indicating that the formation of the CeO_2/ZIS heterojunction considerably inhibits the recombination of photogenerated carriers. For the PEC measurement, the significantly enhanced photocurrent density (Fig. 4c) of the 15% CeO_2/ZIS sample strongly shows the promoted transfer kinetics of photoexcited electron-hole pairs. However, the EIS result (Fig. 4d) shows that the 15% CeO_2/ZIS sample manifests a small semicircle in the Nyquist plots, indicating a low charge transfer resistance. The aforementioned results indicate that the PEC performance of CeO_2/ZIS is dependent on the heterostructure composition.

DFT calculations and EPR experiments
To reveal the Z-scheme mechanism, DFT calculations were conducted to calculate the electrostatic potentials of pure CeO_2 and ZIS, as shown in Fig. 5a, b, respectively. The theoretical calculation is based on the lattice structure models of these two materials (insets in Fig. 5a, b). In terms of the electrostatic potential distribution, the work functions of CeO_2 and ZIS are calculated to be 6.19 and 5.68 eV by comparing their vacuum levels (E_{vac}). The relationship between E_{vac} and Fermi level (E_F) can be expressed as follows:
$$\varphi = E_{vac} - E_F. \quad (3)$$

Assuming that the vacuum energy level is 0 V, the Fermi level of ZIS (−5.68 V) is higher than that of CeO_2 (−6.19 V), which is consistent with the results of the M-S plots (Fig. 2d). Because of the difference in their Fermi levels, free electrons spontaneously migrated from ZIS to CeO_2, resulting in an internal (or built-in) field at the heterogeneous interface. Moreover, the divergence of the charge density of the CeO_2/ZIS heterostructure is illustrated

in Fig. 5c to reveal the charge distribution. The yellow and cyan symbols around the CeO_2/ZIS interface represent accumulated and depleted electrons, respectively. Similar to the p-n junction, the internal electric field contributes to the spatial separation of photogenerated electrons and holes.

In addition to the aforementioned theoretical calculation, the EPR experiment was conducted to monitor the generation of superoxide radicals ($\cdot O_2^-$) and hydroxyl radicals ($\cdot OH$) during the photocatalytic reaction. 5,5-Dimethyl-*L*-pyrroline N-oxide (DMPO) was used to trap $\cdot O_2^-$ and $\cdot OH$, leading to the production of DMPO-$\cdot O_2^-$ and DMPO-$\cdot OH$ in an aqueous solution. As shown in Fig. 5d, the CeO_2 sample shows the weakest EPR signal of DMPO-$\cdot O_2^-$, whereas ZIS exhibits a slightly stronger signal than CeO_2, indicating that the CB position of ZIS is higher than that of CeO_2. Note that the CeO_2/ZIS composite exhibits a clear EPR signal of DMPO-$\cdot O_2^-$, indicating its high catalytic activity for producing $\cdot O_2^-$. However, Fig. 5e shows that ZIS has a higher EPR signal of DMPO-$\cdot OH$ than CeO_2, which can be attributed to the considerable recombination of photoexcited holes in pure CeO_2. The peak intensity of the CeO_2/ZIS composite is high, indicating that holes are retained in the VB of CeO_2 upon composite formation.

To confirm the transfer path of photogenerated carriers, the photocatalytic degradation experiments were conducted on the CeO_2, ZIS, and CeO_2/ZIS samples. Fig. S7a shows the comparison of the photocatalytic activity of the three samples for MB degradation, and Fig. S7b shows the corresponding rate constant *k* of different samples during the degradation process. After 1.5 h of light irradiation, the CeO_2/ZIS sample exhibits a higher photodegradation rate than pure CeO_2 and ZIS, which is consistent with the EPR signal of DMPO-$\cdot OH$. Although CeO_2 has a
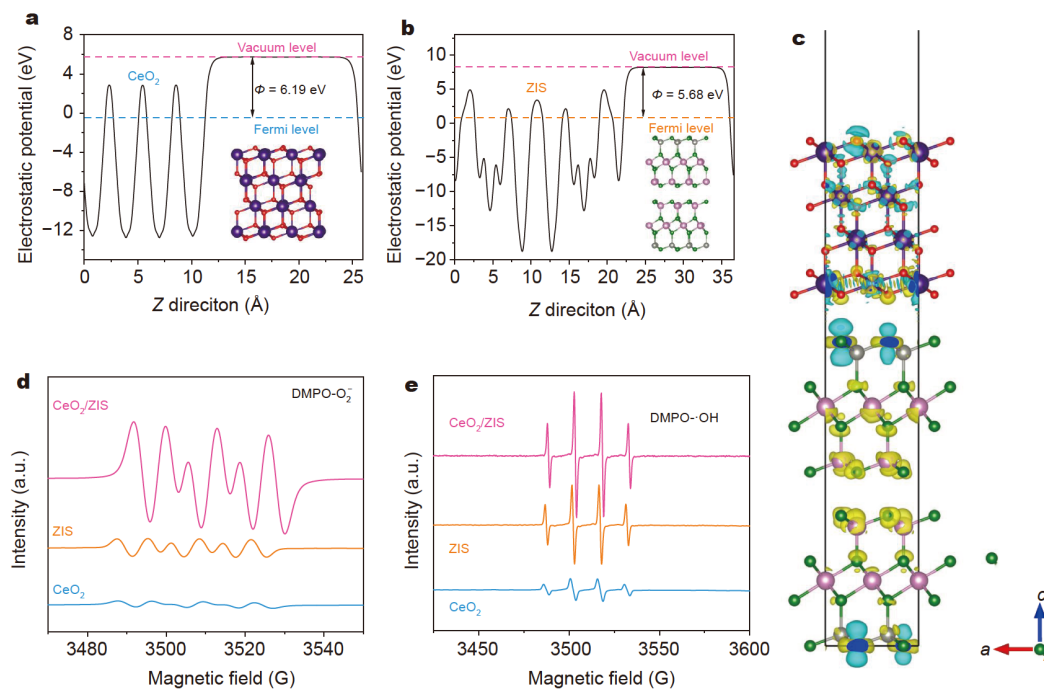
Figure 5 Calculated electrostatic potentials and crystal structures of (a) CeO_2 and (b) ZIS. (c) Divergence of the charge density of CeO_2/ZIS. The EPR spectra of (d) DMPO-·O^{2-} and (e) DMPO-·OH trapped by DMPO in the CeO_2, ZIS, and CeO_2/ZIS dispersion solution.

lower VB position than ZIS, its photocatalytic oxidation activity is limited by a short carrier lifetime.

If the carrier transfer at the CeO_2/ZIS interface follows a Type II heterojunction behavior, the photogenerated electrons will be transferred from ZIS to CeO_2. Consequently, after the formation of a heterojunction, the reduction capability will be considerably reduced because the CB position of CeO_2 is lower than that of ZIS. However, the experimental results indicate that the CeO_2/ZIS hybrid photocatalyst has a higher photocatalytic H_2 evolution performance than CeO_2. This result excludes the possibility of forming a Type II heterojunction. Thus, the electron transfer between ZIS and CeO_2 probably follows the Z-scheme mechanism. In particular, the photogenerated electrons are preserved in the CB of ZIS, whereas the photogenerated holes are retained in the VB of CeO_2, resulting in the superior photocatalytic activity of CeO_2/ZIS for H_2 evolution compared with that of single components such as CeO_2 or ZIS.

KPFM investigation
As a spatially resolved and powerful tool, KPFM is always used to exploit the surface potential and local work function of nanostructures. In this study, KPFM is employed to analyze the surface morphology and corresponding surface potential mapping to obtain an in-depth understanding of the interfacial charge transfer pathway between CeO_2 (A) and ZIS (B). As shown in Fig. 6a, both ZIS NS and CeO_2 NR are distinguished by their topographic structures, and Points A and B represent CeO_2 and ZIS with the heights of 10 and 4 nm, respectively. The surface potential of Point A was determined to be ~30 mV higher than that of Point B (Fig. 6b), resulting in the transfer of free electrons from Point B to Point A [43]. That is, in the region near the CeO_2/ZIS interface, CeO_2 is severely negatively charged, whereas ZIS is positively charged, resulting in the formation of a

built-in field from ZIS to CeO_2.

***In situ* irradiated XPS analysis**
Fig. 7 shows the ordinary and *in situ* irradiated XPS results of the CeO_2, ZIS, and CeO_2/ZIS samples to reveal the surface elemental composition and migration of photoexcited electrons. The *in situ* irradiated XPS measurements were conducted under a 450-nm LED irradiation. Note that the XPS survey spectrum of CeO_2/ZIS confirms the coexistence of Ce, O, Zn, In, and S (Fig. S8). Fig. 7a shows the high-resolution O 1s spectrum with two peaks at 529.0 and 530.9 eV corresponding to the lattice oxygen and adsorbed oxygen in CeO_2 [44,45]. Moreover, eight peaks are detected in the Ce 3d spectra of all of the samples *via* Gaussian fitting (Fig. 7b). Of them, u and v are assigned to Ce $3d_{3/2}$ and Ce $3d_{5/2}$, respectively [46]. The peaks at v, v″, v‴ and u, u″, u‴ can be assigned to Ce^{4+}, whereas the peaks located at 884.58 and 903.02 eV marked as v′ and u′ can be assigned to Ce^{3+} [47–50]. Fig. 7c shows the high-resolution S 2p spectra, where two ZIS peaks at 162.83 and 161.84 eV refer to S $2p_{1/2}$ and S $2p_{3/2}$ corresponding to the S–Zn and/or S–In bonds [51]. Note that the binding energies of Ce 3d and O 1s in CeO_2/ZIS show a negative shift compared with that of pure CeO_2. However, the S 2p peaks in CeO_2/ZIS positively shift by 0.34 eV compared with that in ZIS to balance the electron distribution in the CeO_2/ZIS heterojunction. The shift in binding energies indicates electron transfer from ZIS to CeO_2, which leads to the negative shift of S 2p and the positive shift of O 1s. This result is consistent with the charge transfer pathway monitored by KPFM [52,53]. Note that the peaks of Ce 3d and O 1s in CeO_2/ZIS positively shift after irradiation with a 450-nm LED, whereas considerable negative shifts are observed in the peaks of S 2p, Zn 2p (Fig. 7d), and In 3d (Fig. 7e) [54–57]. The shift of the binding energies shows that the 450-nm LED irradiation decreases the electron
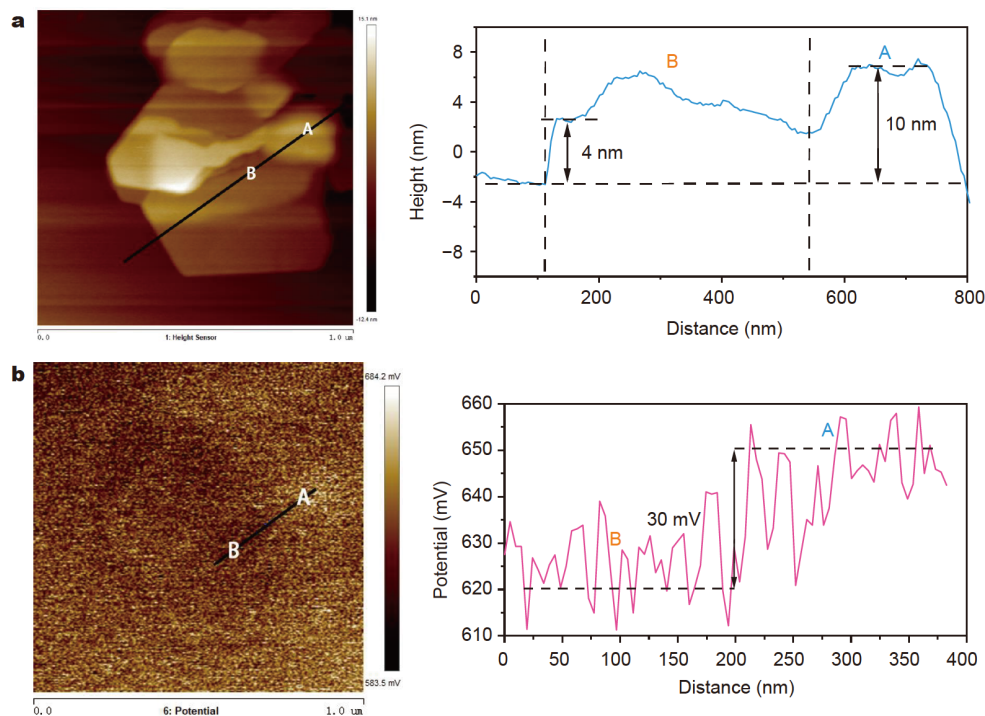
Figure 6 KPFM study of the CeO$_2$/ZIS hybrid. (a) AFM image and corresponding height profile of CeO$_2$/ZIS. (b) Surface potential distribution and line-scanning surface potential from Point A to Point B of CeO$_2$/ZIS.
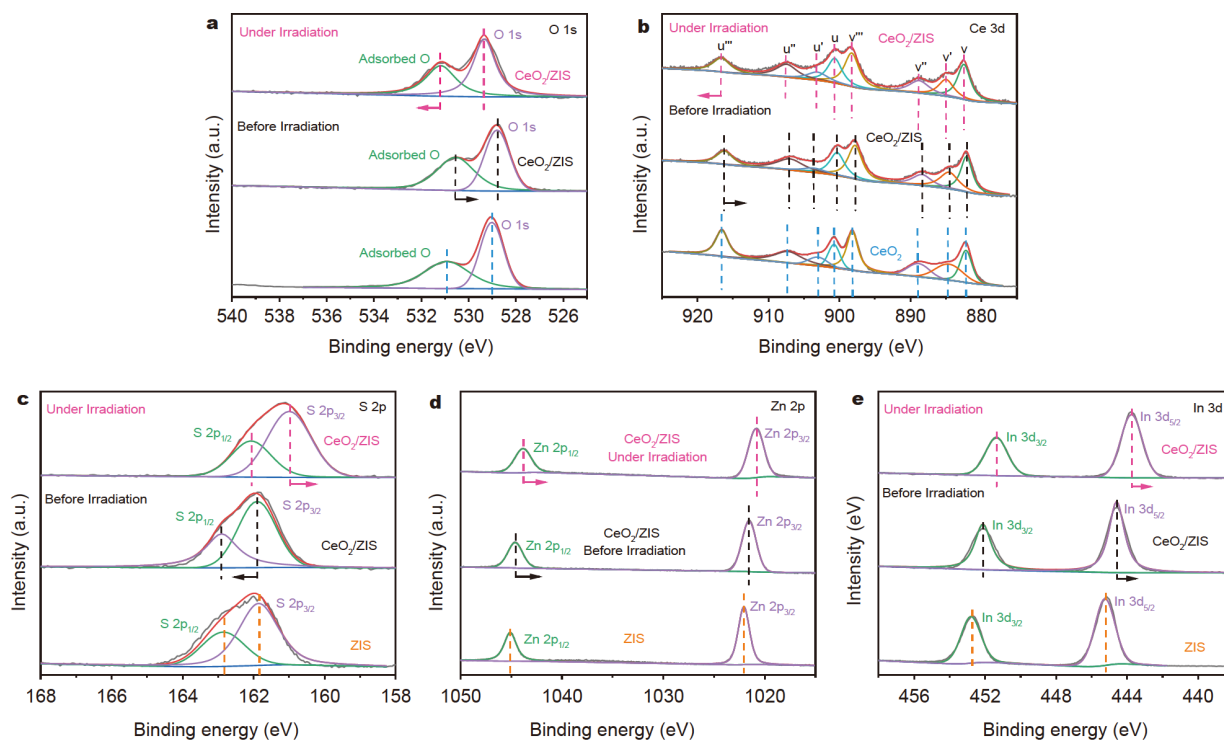

Figure 7 Ordinary and *in situ* irradiated XPS spectra of (a) O 1s, (b) Ce 3d, (c) S 2p, (d) Zn 2p, and (e) In 3d of CeO$_2$, ZIS, and CeO$_2$/ZIS.

density of CeO$_2$ and increases the electron density of ZIS in the CeO$_2$/ZIS heterojunction. Moreover, the electron transfer from CeO$_2$ to ZIS under irradiation is completely opposite to the electron transfer in the dark. Thus, the *in situ* XPS analysis provides direct evidence that the photogenerated electron in the

CeO$_2$/ZIS heterojunction follows the Z-scheme transfer pathway, as will be discussed subsequently using the schematic model.

Possible mechanism for enhanced performance
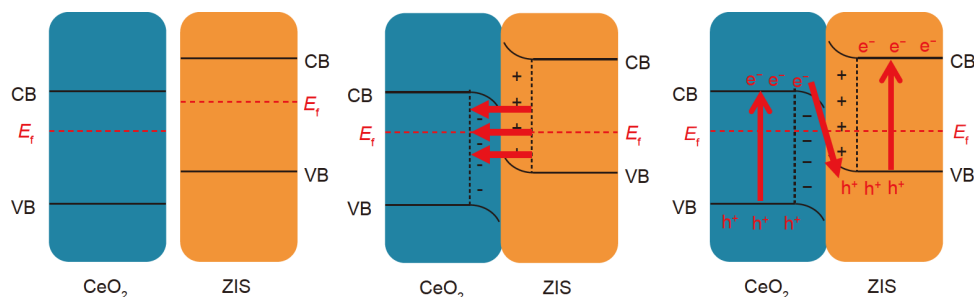Based on the aforementioned results, Fig. 8 shows the proposed

Figure 8 Schematic of the Z-scheme charge transfer process in the CeO$_2$/ZIS heterojunction: (a) before contact, (b) after contact, and (c) after contact under irradiation.

mechanism for carrier migration in CeO$_2$/ZIS. Classified by band structures, CeO$_2$ can be sorted in the OP in which the photogenerated holes are the contributing factors, whereas the photogenerated electrons are the hindering factors (Fig. 8a). However, ZIS acts as RP having higher CB and VB positions than CeO$_2$. When they are in close contact (Fig. 8b), free electrons in ZIS are spontaneously transferred to CeO$_2$ across their interface. Consequently, ZIS is positively charged because of the loss of electrons, whereas CeO$_2$ is negatively charged because of the accumulation of electrons, resulting in the formation of an internal electric field from ZIS to CeO$_2$. This internal field provides a driving force for migrating photogenerated carriers, leading to band bending at their interface because of electron redistribution. Because ZIS and CeO$_2$ in contact should be aligned to the same Fermi level, the edges of their bands at the interface should bend upward and downward (Fig. 8c). This phenomenon can be described as "water flows downward", leading to the recombination of photogenerated electrons in the CB of CeO$_2$ with the holes in the VB of ZIS under irradiation. Furthermore, the powerful photogenerated electrons and holes are reserved in the CB of ZIS and VB of CeO$_2$ to engage in the reduction and oxidation reactions, respectively. Finally, the Z-scheme heterojunction is formed and shows a higher photocatalytic activity for H$_2$ evolution compared with a single component.

CONCLUSIONS

In this work, the hierarchical CeO$_2$/ZIS Z-scheme heterojunction photocatalyst was successfully prepared by *in situ* growth of ultrathin ZIS NSs on the CeO$_2$ NR surface. The H$_2$ production activity of the optimal heterojunction photocatalyst was ~2.7 and 92.6 times higher than that of pure ZIS and CeO$_2$, respectively. Both KPFM measurement and DFT calculation demonstrated the difference in the Fermi levels of the two components, leading to the formation of the internal electric field at the heterogeneous interface. Moreover, the electronic migration from CeO$_2$ to ZIS is systematically demonstrated by EPR and *in situ* XPS characterizations. Hence, the Z-scheme heterojunction was successfully formed between CeO$_2$ and ZIS, leading to enhanced photocatalytic HER performance. This work provides novel insights into the design and fabrication of novel heterojunction photocatalysts, which might be an important step forward in developing their photocatalytic applications.

1   Ran J, Zhang J, Yu J, *et al.* Earth-abundant cocatalysts for semi-conductor-based photocatalytic water splitting. Chem Soc Rev, 2014, 43: 7787–7812

2   Çelik D, Yıldız M. Investigation of hydrogen production methods in accordance with green chemistry principles. Int J Hydrogen Energy, 2017, 42: 23395–23401

3   Wang Z, Li C, Domen K. Recent developments in heterogeneous photocatalysts for solar-driven overall water splitting. Chem Soc Rev, 2019, 48: 2109–2125

4   Lewis NS. Research opportunities to advance solar energy utilization. Science, 2016, 351: aad1920

5   Kudo A, Miseki Y. Heterogeneous photocatalyst materials for water splitting. Chem Soc Rev, 2009, 38: 253–278

6   Shen R, Ren D, Ding Y, *et al.* Nanostructured CdS for efficient photocatalytic H$_2$ evolution: A review. Sci China Mater, 2020, 63: 2153–2188

7   Fujishima A, Honda K. Electrochemical photolysis of water at a semiconductor electrode. Nature, 1972, 238: 37–38

8   Hisatomi T, Domen K. Reaction systems for solar hydrogen production *via* water splitting with particulate semiconductor photocatalysts. Nat Catal, 2019, 2: 387–399

9   Xiao F, Zhou W, Sun B, *et al.* Engineering oxygen vacancy on rutile TiO$_2$ for efficient electron-hole separation and high solar-driven photocatalytic hydrogen evolution. Sci China Mater, 2018, 61: 822–830

10 Ma B, Zhao J, Ge Z, *et al.* 5 nm NiCoP nanoparticles coupled with g-C$_3$N$_4$ as high-performance photocatalyst for hydrogen evolution. Sci China Mater, 2020, 63: 258–266

11 Zhu Y, Wang L, Liu Y, *et al.* *In-situ* hydrogenation engineering of ZnIn$_2$S$_4$ for promoted visible-light water splitting. Appl Catal B-Environ, 2019, 241: 483–490

12 Liu J, Fang W, Wei Z, *et al.* Metallic 1T-Li$_x$MoS$_2$ co-catalyst enhanced photocatalytic hydrogen evolution over ZnIn$_2$S$_4$ floriated microspheres under visible light irradiation. Catal Sci Technol, 2018, 8: 1375–1382

13 Yang W, Zhang L, Xie J, *et al.* Enhanced photoexcited carrier separation in oxygen-doped ZnIn$_2$S$_4$ nanosheets for hydrogen evolution. Angew Chem Int Ed, 2016, 55: 6716–6720

14 Li W, Lin Z, Yang G. A 2D self-assembled MoS$_2$/ZnIn$_2$S$_4$ heterostructure for efficient photocatalytic hydrogen evolution. Nanoscale, 2017, 9: 18290–18298

15 Wang S, Wang Y, Zhang SL, *et al.* Supporting ultrathin ZnIn$_2$S$_4$ nanosheets on Co/N-doped graphitic carbon nanocages for efficient photocatalytic H$_2$ generation. Adv Mater, 2019, 31: 1903404

16 Ye L, Wen Z, Li Z, *et al.* Hierarchical architectured ternary nanostructures photocatalysts with In(OH)$_3$ nanocube on ZnIn$_2$S$_4$/NiS nanosheets for photocatalytic hydrogen evolution. Sol RRL, 2020, 4: 2000027

17 Shi X, Mao L, Dai C, *et al.* Inert basal plane activation of two-dimensional ZnIn$_2$S$_4$ *via* Ni atom doping for enhanced co-catalyst free photocatalytic hydrogen evolution. J Mater Chem A, 2020, 8: 13376–13384

18 Shi X, Dai C, Wang X, *et al.* Protruding Pt single-sites on hexagonal ZnIn$_2$S$_4$ to accelerate photocatalytic hydrogen evolution. Nat Commun, 2022, 13: 1287

19 Jiang R, Mao L, Zhao Y, *et al.* Spatial carrier separation in cobalt phosphate deposited ZnIn$_2$S$_4$ nanosheets for efficient photocatalytic hydrogen evolution. J Colloid Interface Sci, 2022, 606: 317–327

20 Cai X, Zeng Z, Liu Y, *et al.* Visible-light-driven water splitting by yolk-shelled $ZnIn_2S_4$-based heterostructure without noble-metal co-catalyst and sacrificial agent. Appl Catal B-Environ, 2021, 297: 120391

21 Wu K, Mao L, Gu X, *et al.* Efficient charge separation in hierarchical $NiS@ZnIn_2S_4$ hollow nanospheres for photocatalytic water splitting. Chin Chem Lett, 2021, 33: 926–929

22 Jourshabani M, Shariatinia Z, Badiei A. High efficiency visible-light-driven $Fe_2O_{3-x}S$/S-doped g-C_3N_4 heterojunction photocatalysts: Direct Z-scheme mechanism. J Mater Sci Tech, 2018, 34: 1511–1525

23 Majhi D, Das K, Bariki R, *et al.* A facile reflux method for *in situ* fabrication of a non-cytotoxic Bi_2S_3/β-$Bi_2O_3/ZnIn_2S_4$ ternary photocatalyst: A novel dual Z-scheme system with enhanced multifunctional photocatalytic activity. J Mater Chem A, 2020, 8: 21729–21743

24 He X, Zhang C. Recent advances in structure design for enhancing photocatalysis. J Mater Sci, 2019, 54: 8831–8851

25 Di T, Xu Q, Ho WK, *et al.* Review on metal sulphide-based Z-scheme photocatalysts. ChemCatChem, 2019, 11: 1394–1411

26 Zong X, Jiang W, Sun Z. Efficient photocatalytic overall water splitting achieved with polymeric semiconductor-based Z-scheme heterostructures. Sci China Chem, 2021, 64: 875–876

27 Li Y, Ruan Q, Lin H, *et al.* Unique $Cd_{1-x}Zn_xS@WO_{3-x}$ and $Cd_{1-x}Zn_xS@WO_{3-x}/CoO_x/NiO_x$ Z-scheme photocatalysts for efficient visible-light-induced H_2 evolution. Sci China Mater, 2020, 63: 75–90

28 Zhao Z, Xing Y, Li H, *et al.* Constructing CdS/Cd/doped TiO_2 Z-scheme type visible light photocatalyst for H_2 production. Sci China Mater, 2018, 61: 851–860

29 Luo D, Peng L, Wang Y, *et al.* Highly efficient photocatalytic water splitting utilizing a $WO_{3-x}/ZnIn_2S_4$ ultrathin nanosheet Z-scheme catalyst. J Mater Chem A, 2021, 9: 908–914

30 He F, Zhu B, Cheng B, *et al.* 2D/2D/0D $TiO_2/C_3N_4/Ti_3C_2$ MXene composite S-scheme photocatalyst with enhanced CO_2 reduction activity. Appl Catal B-Environ, 2020, 272: 119006

31 Kusmierek E. A CeO_2 semiconductor as a photocatalytic and photoelectrocatalytic material for the remediation of pollutants in industrial wastewater: A review. Catalysts, 2020, 10: 1435

32 Cai X, Su M, Zeng Z, *et al.* Boosting the photocatalytic H_2 evolution activity of a CdS/N-doped $ZnIn_2S_4$ direct Z-scheme heterostructure using a band alignment regulation strategy. Sustain Energy Fuels, 2021, 5: 6441–6448

33 Li Q, Song L, Liang Z, *et al.* A review on CeO_2-based electrocatalyst and photocatalyst in energy conversion. Adv Energy Sustain Res, 2021, 2: 2000063

34 Wang K, Liu S, Zhang L, *et al.* Hierarchically grown Ni-Mo-S modified 2D CeO_2 for high-efficiency photocatalytic hydrogen evolution. Catal Lett, 2022, 152: 931–943

35 Ebadi M, Teymourinia H, Amiri O, *et al.* Synthesis of CeO_2/Ag/Ho nanostructures in order to improve photo catalytic activity of CeO_2 under visible light. J Mater Sci-Mater Electron, 2018, 29: 8817–8821

36 Zhou K, Yang Z, Yang S. Highly reducible CeO_2 nanotubes. Chem Mater, 2007, 19: 1215–1217

37 Trovarelli A, Llorca J. Ceria catalysts at nanoscale: How do crystal shapes shape catalysis? ACS Catal, 2017, 7: 4716–4735

38 Tian J, Sang Y, Zhao Z, *et al.* Enhanced photocatalytic performances of CeO_2/TiO_2 nanobelt heterostructures. Small, 2013, 9: 3864–3872

39 Wang S, Guan BY, Lou XWD. Construction of $ZnIn_2S_4$-In_2O_3 hierarchical tubular heterostructures for efficient CO_2 photoreduction. J Am Chem Soc, 2018, 140: 5037–5040

40 Zhang M, Yao J, Arif M, *et al.* 0D/2D $CeO_2/ZnIn_2S_4$ Z-scheme heterojunction for visible-light-driven photocatalytic H_2 evolution. Appl Surf Sci, 2020, 526: 145749

41 Zeng C, Hu Y, Huang H. $BiOBr_{0.75}I_{0.25}/BiOIO_3$ as a novel heterojunctional photocatalyst with superior visible-light-driven photocatalytic activity in removing diverse industrial pollutants. ACS Sustain Chem Eng, 2017, 5: 3897–3905

42 Shi X, Mao L, Yang P, *et al.* Ultrathin $ZnIn_2S_4$ nanosheets with active (110) facet exposure and efficient charge separation for cocatalyst free photocatalytic hydrogen evolution. Appl Catal B-Environ, 2020, 265: 118616

43 Wang R, Xue J, Wang KL, *et al.* Constructive molecular configurations for surface-defect passivation of perovskite photovoltaics. Science, 2019, 366: 1509–1513

44 She X, Xu H, Wang H, *et al.* Controllable synthesis of CeO_2/g-C_3N_4 composites and their applications in the environment. Dalton Trans, 2015, 44: 7021–7031

45 Zou W, Shao Y, Pu Y, *et al.* Enhanced visible light photocatalytic hydrogen evolution *via* cubic CeO_2 hybridized g-C_3N_4 composite. Appl Catal B-Environ, 2017, 218: 51–59

46 Zhang Y, Zhang N, Tang ZR, *et al.* A unique silk mat-like structured Pd/CeO_2 as an efficient visible light photocatalyst for green organic transformation in water. ACS Sustain Chem Eng, 2013, 1: 1258–1266

47 Bêche E, Charvin P, Perarnau D, *et al.* Ce 3d XPS investigation of cerium oxides and mixed cerium oxide ($Ce_xTi_yO_z$). Surf Interface Anal, 2008, 40: 264–267

48 Hao C, Tang Y, Shi W, *et al.* Facile solvothermal synthesis of a Z-scheme 0D/3D $CeO_2/ZnIn_2S_4$ heterojunction with enhanced photocatalytic performance under visible light irradiation. Chem Eng J, 2021, 409: 128168

49 Zhang P, Liu Y, Tian B, *et al.* Synthesis of core-shell structured $CdS@CeO_2$ and $CdS@TiO_2$ composites and comparison of their photocatalytic activities for the selective oxidation of benzyl alcohol to benzaldehyde. Catal Today, 2017, 281: 181–188

50 Khan MM, Ansari SA, Pradhan D, *et al.* Defect-induced band gap narrowed CeO_2 nanostructures for visible light activities. Ind Eng Chem Res, 2014, 53: 9754–9763

51 Li Z, Wang X, Tian W, *et al.* CoNi bimetal cocatalyst modifying a hierarchical $ZnIn_2S_4$ nanosheet-based microsphere noble-metal-free photocatalyst for efficient visible-light-driven photocatalytic hydrogen production. ACS Sustain Chem Eng, 2019, 7: 20190–20201

52 Zhu Q, Sun Y, Xu S, *et al.* Rational design of 3D/2D In_2O_3 nanocube/$ZnIn_2S_4$ nanosheet heterojunction photocatalyst with large-area "high-speed channels" for photocatalytic oxidation of 2,4-dichlorophenol under visible light. J Hazard Mater, 2020, 382: 121098

53 Chen Y, Tian G, Ren Z, *et al.* Hierarchical core-shell carbon nanofiber@$ZnIn_2S_4$ composites for enhanced hydrogen evolution performance. ACS Appl Mater Interfaces, 2014, 6: 13841–13849

54 Qin Y, Li H, Lu J, *et al.* Synergy between van der Waals heterojunction and vacancy in $ZnIn_2S_4$/g-C_3N_4 2D/2D photocatalysts for enhanced photocatalytic hydrogen evolution. Appl Catal B-Environ, 2020, 277: 119254

55 Qin Y, Li H, Lu J, *et al.* Photocatalytic degradation of 2-mercaptobenzothiazole by a novel Bi_2WO_6 nanocubes/$In(OH)_3$ photocatalyst: Synthesis process, degradation pathways, and an enhanced photocatalytic performance mechanism study. Appl Surf Sci, 2019, 481: 1313–1326

56 Tian N, Huang H, Liu C, *et al. In situ* co-pyrolysis fabrication of CeO_2/g-C_3N_4 n-n type heterojunction for synchronously promoting photoinduced oxidation and reduction properties. J Mater Chem A, 2015, 3: 17120–17129

57 Chen L, Meng D, Wu X, *et al. In situ* synthesis of V^{4+} and Ce^{3+} self-doped $BiVO_4/CeO_2$ heterostructured nanocomposites with high surface areas and enhanced visible-light photocatalytic activity. J Phys Chem C, 2016, 120: 18548–18559

Author contributions   Jiang R performed the experiments and wrote the paper with support from Chubenko EB and Bondarenko V; Mao L and Zhao Y designed and engineered the samples; Zhang J and Cai X contributed to the theoretical analysis; Sui Y, Gu X, and Cai X performed the data analysis. All authors contributed to the general discussion.

Conflict of interest   The authors declare that they have no conflict of interest.

Supplementary information   Supporting data are available in the online version of the paper.

Renqian Jiang received her BS degree from Central South University. She is currently studying for her MS degree under the supervision of Professor Xiuquan Gu at the University of Mining and Technology. Her research interest focuses on photocatalytic hydrogen production.

Xiuquan Gu received his BS degree in physics from Anhui Normal University and his PhD degree from Zhejiang University in 2009. He is currently an assistant professor at the University of Mining and Technology. His current research interests include semiconductor photocatalysis, photocatalytic hydrogen production, and photoelectrocatalysis.

Xiaoyan Cai received her PhD degree from Beihang University in 2018. She is currently a faculty member at the School of Materials Science and Physics, China University of Mining and Technology. Her research interests are photocatalytic and electrocatalytic materials for energy conversion and environmental remediation.

1D/2D CeO₂/ZnIn₂S₄ Z-scheme异质结光催化剂实现高效可见光分解水制氢

姜人倩[1,2], 毛梁[1,2], 赵宇龙[1,2], 张俊英[3], Eugene B. Chubenko[4], Vitaly Bondarenko[4], 隋艳伟[1,2], 顾修全[1,2*], 蔡晓燕[1,2*]

摘要 开发具有高效电荷转移效率的光催化剂已成为太阳能-氢能转换的关键科学方法. 本研究通过在CeO₂纳米棒表面原位生长ZnIn₂S₄纳米片，成功制备了具有Z-scheme异质结的1D/2D CeO₂/ZnIn₂S₄光催化剂. 在无助催化剂的情况下, 15 wt% CeO₂/85 wt% ZnIn₂S₄样品在可见光下实现了 $3.29\ \mathrm{mmol\ g^{-1}\ h^{-1}}$ 的最佳H₂产量，该值分别比原始ZnIn₂S₄和CeO₂分别高2.7倍和92.6倍. 优异的光催化活性可能是由于光生载流子的有效分离和Z-scheme异质结的形成保留了ZnIn₂S₄中用于产氢的强还原电子. 密度泛函理论计算和开尔文探针力显微镜证明了CeO₂和ZnIn₂S₄之间存在内部电场. 此外，电子顺磁共振光谱以及原位辐照X射线光电子能谱证实了CeO₂/ZnIn₂S₄异质结中的光生载流子按照Z-scheme路径转移. 这项工作可为开发用于太阳能水分解制氢的高效Z-scheme光催化剂提供一些见解.